The Astronomical Journal, 158:28 (13pp), 2019 July https://doi.org/10.3847/1538-3881/ab237f

Spitzer Parallax of OGLE-2018-BLG-0596: A Low-mass-ratio Planet around an M Dwarf

Youn Kil Jung[1,35], Andrew Gould[1,2,3,35,37], Andrzej Udalski[4,36], Takahiro Sumi[5,38], Jennifer C. Yee[6,35,37], Yossi Shvartzvald[7,35,37,39], Weicheng Zang[8,35,37,40],
and
Cheongho Han[9,35], Michael D. Albrow[10], Sun-Ju Chung[1,11], Kyu-Ha Hwang[1], Yoon-Hyun Ryu[1], In-Gu Shin[1], Wei Zhu[12,37,40], Sang-Mok Cha[1,13], Dong-Jin Kim[1], Hyoun-Woo Kim[1], Seung-Lee Kim[1,11], Chung-Uk Lee[1,11], Dong-Joo Lee[1], Yongseok Lee[1,13], Byeong-Gon Park[1,11], Richard W. Pogge[2]
(The KMTNet Collaboration),
Przemek Mróz[4], Michał K. Szymański[4], Jan Skowron[4], Radek Poleski[2], Igor Soszyński[4], Paweł Pietrukowicz[4], Szymon Kozłowski[4], Krzysztof Ulaczyk[14], Krzysztof A. Rybicki[4], Patryk Iwanek[4], Marcin Wrona[4]
(The OGLE Collaboration),
Charles A. Beichman[15,39], Geoffery Bryden[16,39], Sebastiano Calchi Novati[7,39], Sean Carey[17], B. Scott Gaudi[2,39], Calen B. Henderson[7,39]
(The Spitzer Team),
Fumio Abe[18], Richard Barry[19], David P. Bennett[19,20], Ian A. Bond[21], Aparna Bhattacharya[19,20], Martin Donachie[22], Akihiko Fukui[23,24], Yuki Hirao[5], Yoshitaka Itow[18], Iona Kondo[5], Naoki Koshimoto[25,26], Man Cheung Alex Li[22], Yutaka Matsubara[18], Shota Miyazaki[5], Yasushi Muraki[18], Masayuki Nagakane[5], Clément Ranc[19], Nicholas J. Rattenbury[22], Haruno Suematsu[5], Denis J. Sullivan[27], Daisuke Suzuki[28], Paul J. Tristram[29], Atsunori Yonehara[30]
(The MOA Collaboration),
Savannah Jacklin[31], Matthew T. Penny[2,40], Keivan G. Stassun[31]
(The UKIRT Microlensing Team),
and
Pascal Fouqué[32,33], Shude Mao[8,34], and Tianshu Wang[8]
(The CFHT Microlensing Collaboration)

[1] Korea Astronomy and Space Science Institute, Daejon 34055, Republic of Korea
[2] Department of Astronomy, Ohio State University, 140 W. 18th Ave., Columbus, OH 43210, USA
[3] Max-Planck-Institute for Astronomy, Königstuhl 17, D-69117 Heidelberg, Germany
[4] Warsaw University Observatory, Al. Ujazdowskie 4, 00-478 Warszawa, Poland
[5] Department of Earth and Space Science, Graduate School of Science, Osaka University, Toyonaka, Osaka 560-0043, Japan
[6] Center for Astrophysics | Harvard & Smithsonian, 60 Garden Street, Cambridge, MA 02138, USA
[7] IPAC, Mail Code 100-22, Caltech, 1200 E. California Boulevard, Pasadena, CA 91125, USA
[8] Physics Department and Tsinghua Centre for Astrophysics, Tsinghua University, Beijing 100084, People's Republic of China
[9] Department of Physics, Chungbuk National University, Cheongju 28644, Republic of Korea
[10] University of Canterbury, Department of Physics and Astronomy, Private Bag 4800, Christchurch 8020, New Zealand
[11] University of Science and Technology, Korea, 217 Gajeong-ro Yuseong-gu, Daejeon 34113, Republic of Korea
[12] Canadian Institute for Theoretical Astrophysics, University of Toronto, 60 St. George Street, Toronto, ON M5S 3H8, Canada
[13] School of Space Research, Kyung Hee University, Yongin 17104, Republic of Korea
[14] Department of Physics, University of Warwick, Gibbet Hill Road, Coventry, CV4 7AL, UK
[15] NASA Exoplanet Science Institute, MS 100-22, California Institute of Technology, Pasadena, CA 91125, USA
[16] Jet Propulsion Laboratory, California Institute of Technology, 4800, Oak Grove Dr., Pasadena, CA 91109, USA
[17] Spitzer Science Center, MS 220-6, California Institute of Technology, Pasadena, CA, USA
[18] Institute for Space-Earth Environmental Research, Nagoya University, Nagoya 464-8601, Japan
[19] Code 667, NASA Goddard Space Flight Center, Greenbelt, MD 20771, USA
[20] Department of Astronomy, University of Maryland, College Park, MD 20742, USA
[21] Institute of Natural and Mathematical Science, Massey University, Auckland 0745, New Zealand
[22] Department of Physics, University of Auckland, Private Bag 92019, Auckland, New Zealand
[23] Department of Earth and Planetary Science, Graduate School of Science, The University of Tokyo, 7-3-1 Hongo, Bunkyo-ku, Tokyo 113-0033, Japan
[24] Instituto de Astrofísica de Canarias, Vía Láctea s/n, E-38205 La Laguna, Tenerife, Spain
[25] Department of Astronomy, Graduate School of Science, The University of Tokyo, 7-3-1 Hongo, Bunkyo-ku, Tokyo 113-0033, Japan
[26] National Astronomical Observatory of Japan, 2-21-1 Osawa, Mitaka, Tokyo 181-8588, Japan
[27] School of Chemical and Physical Science, Victoria University, Wellington, New Zealand
[28] Institute of Space and Astronautical Science, Japan Aerospace Exploration Agency, Kanagawa 252-5210, Japan
[29] University of Canterbury Mt. John Observatory, P.O. Box 56, Lake Tekapo 8770, New Zealand
[30] Department of Physics, Faculty of Science, Kyoto Sangyo University, Kyoto 603-8555, Japan
[31] Vanderbilt University, Department of Physics & Astronomy, PMB 401807, 2301 Vanderbilt Place, Nashville, TN 37235, USA
[32] CFHT Corporation, 65-1238 Mamalahoa Highway, Kamuela, HI 96743, USA

[33] Université de Toulouse, UPS-OMP, IRAP, Toulouse, France
[34] National Astronomical Observatories, Chinese Academy of Sciences, A20 Datun Road, Chaoyang District, Beijing 100012, People's Republic of China
Received 2019 March 27; revised 2019 May 9; accepted 2019 May 20; published 2019 June 21

Abstract

We report the discovery of a *Spitzer* microlensing planet OGLE-2018-BLG-0596Lb, with preferred planet-host mass ratio $q \sim 2 \times 10^{-4}$. The planetary signal, which is characterized by a short ($\sim$1 day) "bump" on the rising side of the lensing light curve, was densely covered by ground-based surveys. We find that the signal can be explained by a bright source that fully envelops the planetary caustic, i.e., a "Hollywood" geometry. Combined with the source proper motion measured from *Gaia*, the *Spitzer* satellite parallax measurement makes it possible to precisely constrain the lens physical parameters. The preferred solution, in which the planet perturbs the minor image due to lensing by the host, yields a Uranus-mass planet with a mass of $M_{\rm p} = 13.9 \pm 1.6\ M_\oplus$ orbiting a mid M-dwarf with a mass of $M_{\rm h} = 0.23 \pm 0.03\ M_\odot$. There is also a second possible solution that is substantially disfavored but cannot be ruled out, for which the planet perturbs the major image. The latter solution yields $M_{\rm p} = 1.2 \pm 0.2\ M_\oplus$ and $M_{\rm h} = 0.15 \pm 0.02\ M_\odot$. By combining the microlensing and *Gaia* data together with a Galactic model, we find in either case that the lens lies on the near side of the Galactic bulge at a distance $D_{\rm L} \sim 6 \pm 1$ kpc. Future adaptive optics observations may decisively resolve the major image/minor image degeneracy.

Key words: gravitational lensing: micro – planetary systems

1. Introduction

In microlensing events, the principal observable connected to the physical properties of the lens is the Einstein timescale $t_{\rm E}$. However, the timescale results from a combination of the lens mass M and the lens-source relative proper motion $\mu_{\rm rel}$ and parallax $\pi_{\rm rel}$, i.e.,

$$t_{\rm E} = \frac{\theta_{\rm E}}{\mu_{\rm rel}}; \qquad \theta_{\rm E} = \sqrt{\kappa M \pi_{\rm rel}}\,, \tag{1}$$

where $\theta_{\rm E}$ is the angular Einstein radius and

$$\kappa = \frac{4\,{\rm G}}{c^2 {\rm au}} \sim 8.14\ {\rm mas}\ M_\odot^{-1}; \qquad \pi_{\rm rel} = {\rm au}\left(\frac{1}{D_{\rm L}} - \frac{1}{D_{\rm S}}\right). \tag{2}$$

Here, $D_{\rm L}$ and $D_{\rm S}$ are the lens and the source distances, respectively. Therefore, it is difficult to uniquely constrain the lens physical parameters from the timescale alone. To resolve this (M, $\mu_{\rm rel}$, $\pi_{\rm rel}$) degeneracy requires measuring two additional quantities: $\theta_{\rm E}$ and the microlens parallax $\boldsymbol{\pi}_{\rm E}$. The measurements of these two quantities enable one to determine the physical parameters through the relations (Gould 2000)

$$M = \frac{\theta_{\rm E}}{\kappa \pi_{\rm E}}; \qquad \pi_{\rm rel} = \theta_{\rm E} \pi_{\rm E};$$
$$\boldsymbol{\mu}_{\rm rel} = \frac{\theta_{\rm E}}{t_{\rm E}} \frac{\boldsymbol{\pi}_{\rm E}}{\pi_{\rm E}}. \tag{3}$$

Additionally, if the source proper motion $\boldsymbol{\mu}_{\rm S}$ and parallax $\pi_{\rm S} = {\rm au}/D_{\rm S}$ are independently estimated, the $\theta_{\rm E}$ and $\boldsymbol{\pi}_{\rm E}$ measurements allow one to infer the phase-space coordinates of the lens system by

$$\boldsymbol{\mu}_{\rm L} = \boldsymbol{\mu}_{\rm rel} + \boldsymbol{\mu}_{\rm S}; \qquad \pi_{\rm L} = \pi_{\rm rel} + \pi_{\rm S}, \tag{4}$$

where $\boldsymbol{\mu}_{\rm L}$ and $\pi_{\rm L} = {\rm au}/D_{\rm L}$ are the lens proper motion and parallax, respectively.

As summarized by Zhu et al. (2015), there are several approaches for the measurement of $\theta_{\rm E}$, but the most common is to detect the deviation in the observed light curve induced by the extended nature of source stars, i.e., finite-source effects. Such a deviation arises when the source is placed in or near the region where the lensing magnification of a point-like source would diverge to infinity (i.e., a caustic). The detection of the finite-source effect usually returns the source radius normalized to the Einstein radius, $\rho = \theta_*/\theta_{\rm E}$, where θ_* is the angular radius of the source. Because θ_* is routinely measured from the additional information of the source color and magnitude (Yoo et al. 2004), one can determine $\theta_{\rm E}$ provided that ρ is measured from the light curve.

The microlens parallax can be measured through the annual microlens parallax effect. This effect arises from the orbital acceleration of Earth, which displaces the position of an observer relative to rectilinear lens-source motion (Gould 1992). However, the measurement of $\boldsymbol{\pi}_{\rm E}$ in this single accelerating frame is usually difficult because the change of the observer's position during typical microlensing events ($t_{\rm E} < {\rm yr}/2\pi$) is quite minor. As a result, the sample of events with $\boldsymbol{\pi}_{\rm E}$ measured from the annual parallax effect is relatively small, and they are biased toward events with long timescales (e.g., Jung et al. 2019b) and/or events produced by nearby lenses (e.g., Jung et al. 2018a).

The alternative way to measure $\boldsymbol{\pi}_{\rm E}$ is to use a satellite in a heliocentric orbit: the space-based microlens parallax effect. For typical lensing events, the displacement of the satellite from Earth comprises a substantial fraction of the projected Einstein radius $\tilde{r}_{\rm E} = {\rm au}/\pi_{\rm E} \sim 10$ au. In this case, the lensing light curves simultaneously observed from Earth and the satellite can appear to be different because the time-dependent lens-source separation seen from the two observers can be different. Then, one can measure the microlens parallax by comparing these two light curves. This idea was first proposed by Refsdal (1966) a half century ago, and the first such $\boldsymbol{\pi}_{\rm E}$ measurement was made by Dong et al. (2007), in which they analyzed the event OGLE-2005-SMC-001 by using both ground-based and *Spitzer* observations. Subsequently, about a thousand microlensing events have been observed through the *Spitzer* microlensing campaign (Gould et al. 2013, 2014, 2015a, 2015b, 2016, 2018) in order to measure their microlens parallaxes. Combined with ground-based observations, these $\boldsymbol{\pi}_{\rm E}$ measurements have provided a unique opportunity to probe a variety of astrophysical

[35] The KMTNet Collaboration.
[36] The OGLE Collaboration.
[37] The *Spitzer* Team.
[38] The MOA Collaboration.
[39] The UKIRT Microlensing Team.
[40] The CFHT Mircolensing Collaboration.

populations, including binary brown dwarfs (Albrow et al. 2018), single-mass objects (Zhu et al. 2016; Chung et al. 2017; Shin et al. 2018; Shvartzvald et al. 2019), and planetary systems (Udalski et al. 2015b; Street et al. 2016; Shvartzvald et al. 2017b; Calchi Novati et al. 2018, 2019; Ryu et al. 2018).

Here, we analyze the microlensing event OGLE-2018-BLG-0596 and report the discovery of a low-mass-ratio planet orbiting a mid M-dwarf, i.e., with a preferred mass ratio of $q \sim 2 \times 10^{-4}$. The event was observed by several ground-based surveys and *Spitzer*, and the proper motion of the microlensed source was independently measured from *Gaia*. The ground-based observations clearly show a short-term anomaly in the rising part of the light curve, from which the presence of the planet is inferred. Moreover, the parallax measurement from *Spitzer* and the proper motion from *Gaia* allow us to precisely constrain the lens physical properties.

2. Observation

2.1. Ground-based Observations

OGLE-2018-BLG-0596 is at (R.A., decl.)$_{J2000}$ = (17:56:13.33, −29:11:56.7), corresponding to (l, b) = (0.96, −2.13) in Galactic coordinates. It was discovered as a probable microlensing event by the Optical Gravitational Lensing Experiment (OGLE: Udalski et al. 2015a) survey, and announced on 2018 April 15 through its Early Warning System (Udalski 2003). The event is in the OGLE-IV field BLG505, for which OGLE observations were conducted with a one hour cadence using the 1.3 m Warsaw telescope located at Las Campanas in Chile.

The Microlensing Observations in Astrophysics (MOA: Sumi et al. 2003) survey independently discovered this event on May 15 and named it as MOA-2018-BLG-145. The MOA observations were taken using the 1.8 m MOA-II telescope located at Mt. John Observatory in New Zealand. The MOA observation cadence for the event is 15 minutes.

The event was also independently discovered by the Korea Microlensing Telescope Network (KMTNet: Kim et al. 2016) by employing their post-season event finder algorithm (Kim et al. 2018), and it was cataloged as KMT-2018-BLG-0945. The KMTNet survey used three 1.6 m telescopes positioned at the Cerro Tololo Interamerican Observatory, Chile (KMTC), the South African Astronomical Observatory, South Africa (KMTS), and the Siding Spring Observatory, Australia (KMTA). The KMTNet observations were conducted with a 30 minute cadence.

The great majority of images were obtained in the I band for OGLE and KMTNet and a customized R band for MOA,[41] with some V-band images for the source color measurement. All of the survey data were reduced using the image subtraction methodology (Alard & Lupton 1998), specifically Woźniak (2000) for OGLE, Bond et al. (2001) for MOA, and Albrow et al. (2009) for KMTNet.

In addition to the observations from these high-cadence surveys, the event was observed by two lower-cadence surveys. These surveys used, respectively, the 3.8 m United Kingdom Infrared Telescope (UKIRT: Shvartzvald et al. 2017a) and the 3.6 m Canada–France–Hawaii Telescope (CFHT: Zang et al. 2018) that are both located at the Maunakea Observatory in Hawaii. The UKIRT and CFHT observations for the event were carried out in the H and i band, respectively.

[41] MOA survey uses a custom wide-band filter referred as MOA-Red, corresponding to the combination of a standard R- and I-band.

2.2. Spitzer Observations

On May 10, the KMTNet group noticed in KMTNet data reduced on the basis of the OGLE alert that the event had shown an anomaly at HJD′(=HJD − 2,450,000) ∼ 8243.5. Because this anomaly occurred when the event was just ∼0.3 mag brighter than its baseline, it was impossible to precisely determine the lensing parameters at that time. Nevertheless, they found from real-time modeling that the anomaly was likely to have been produced by a very low-mass companion to the primary lens, i.e., a planetary companion. In response to this potential importance, the *Spitzer* team announced OGLE-2018-BLG-0596 as a *Spitzer* target on May 24. The *Spitzer* observations for the event were initiated on July 4 (when it first became observable due to Sun-angle restrictions) with a cadence of 1 day. In total, 36 images were taken during 8304 < HJD′ < 8341. The data were reduced based on the methods presented by Calchi Novati et al. (2015b).

2.2.1. Is the Event Part of the Spitzer Parallax Sample?

The main goal of the *Spitzer* microlensing campaign is to derive the Galactic distribution of planets (Calchi Novati et al. 2015a; Zhu et al. 2017). In order to have an unbiased sample, which is essential to achieve this goal, the events that are included in the experiment must follow strict selection protocols specified by Yee et al. (2015a). Because OGLE-2018-BLG-0596 was selected as a *Spitzer* target significantly after the planetary anomaly, naively it seems that it should immediately be excluded from the sample. However, Yee et al. (2015a) anticipated exactly this situation (an early planetary anomaly) and specified strict selection criteria under which these planets can be included in the sample while keeping it unbiased. For example, OGLE-2016-BLG-1190 (Ryu et al. 2018) also had an early planetary anomaly and is part of the *Spitzer* sample thanks to these protocols.

Yee et al. (2015a) specified two classes of "objective" selection criteria under which an event might be included in the sample: rising events and events that already peaked, i.e., falling events. All events that pass these strict criteria *must* be observed by *Spitzer*. The time threshold between the two classes is $t_0 = t_{dec} - 2$ days, where t_0 is the time of maximum magnification and t_{dec} is the time when *Spitzer* observations are finalized before each observing week. In the case of OGLE-2018-BLG-0596, the first decision date was 2018 June 25, Monday UT 13:25, i.e., $t_{dec} = 8295.06$. Because the event already peaked more than two weeks earlier it should be considered under the criteria for falling events (Section 6.1 of Yee et al. 2015a).

The falling event criteria include six criteria (A1–A6). The first is simply the definition of a falling event, A1: $t_0 > t_{dec} - 2$ days, which in marginal cases needs to be carefully modeled but in the case of OGLE-2018-BLG-0596 was clearly already satisfied. The second criterion is for the event to be in a relatively high-cadence OGLE or KMT field, which as described in Section 2.1 is clearly satisfied. The third criterion requires that the event peaked brighter than A3: $I_{peak} < 17$ mag, which again is clearly satisfied.

The next three are model-dependent criteria and must be examined by (1) using the data that were available to the team at t_{dec} and (2) removing the signature of the planetary anomaly (i.e., excluding the data during 8240 < HJD′ < 8246). In addition, these criteria require the evaluation of the magnification of a single-lens single-source (1L1S) model at two specific

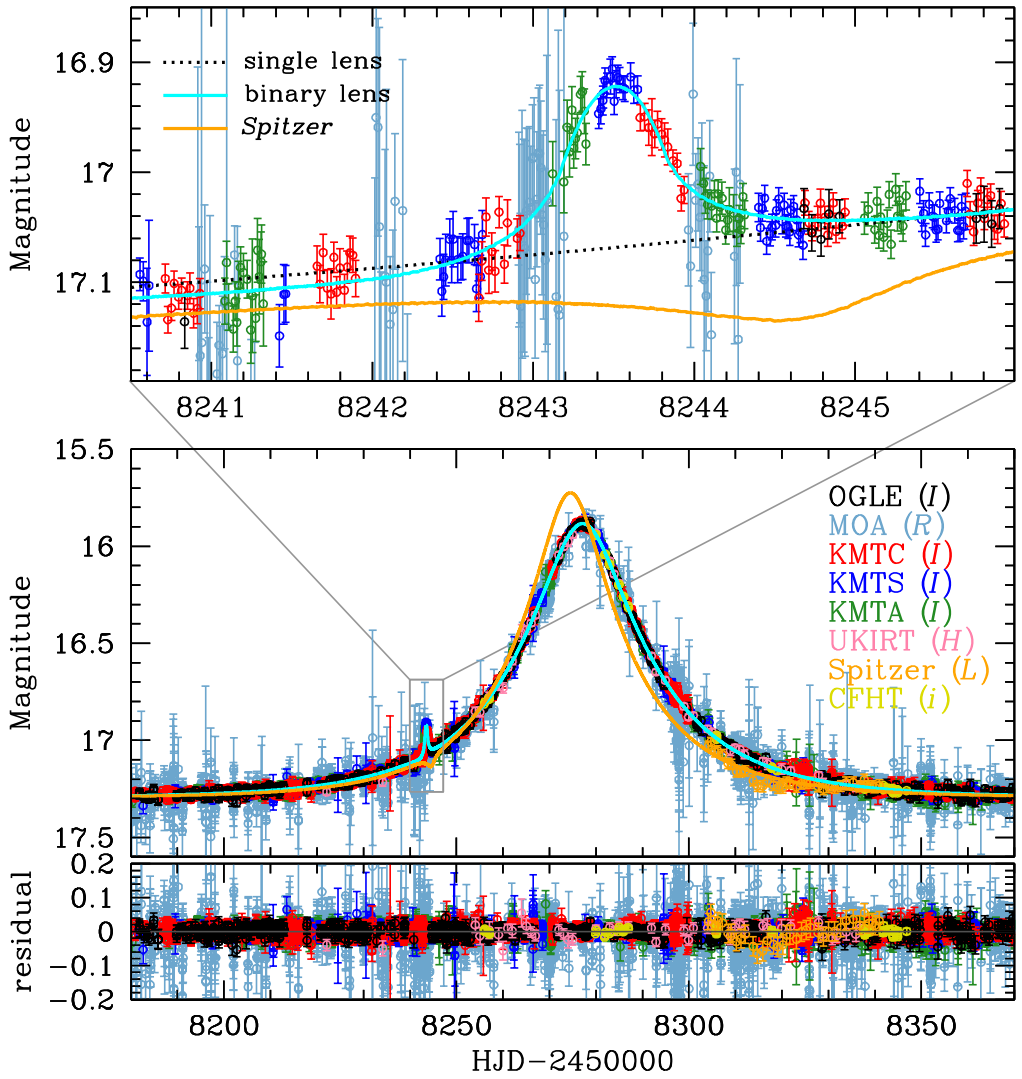

Figure 1. Light curve of OGLE-2018-BLG-0596. The upper panel shows the enlarged view of the anomaly centered at HJD′ ∼ 8243.5. The cyan and orange curves are the best-fit model curves for the ground- and space-based observations, respectively. The black dotted curve is the model curve obtained from the 1L1S interpretation.

times, $t_{\rm next}$ and $t_{\rm fin}$ which are the time of the next (i.e., first) and last possible *Spitzer* observations, respectively. We fit the event to a single-lens event with the online OGLE, MOA, and KMT data that were available to the team by $t_{\rm dec}$, after excluding the anomalous region, and then checked the next criterion. We note that the *Spitzer* team did this examination also immediately after $t_{\rm dec}$, and reached the same conclusions that we find below.

Criterion A4 requires that there will be significant magnification change during the observable *Spitzer* window, A4: $A(t_{\rm next}) - A(t_{\rm fin}) > 0.3$. We find $A(t_{\rm next}) - A(t_{\rm fin}) = 0.29$. We note for completeness that the event easily passes Criterion A5 (that the event will be bright enough to observe from *Spitzer*) and Criterion A6 (that the event will undergo a significant change in magnitude during the *Spitzer* observations). However, because it fails A4, we conclude that OGLE-2018-BLG-0596 does not meet the "objective" selection criteria and cannot be included in the *Spitzer* sample.

3. Analysis

Figure 1 displays the light curve of OGLE-2018-BLG-0596 with the best-fit model. Ignoring the *Spitzer* data, it primarily takes the symmetric form of a standard Paczyński (1986) curve with a magnification $A_{\rm max} \sim 3.6$ at the peak. However, there is a short-lived, weak "bump" on the rising part of the light curve at HJD′ ∼ 8243.5. This appearance could be produced by a "Hollywood" geometry (Gould 1997), i.e., a small caustic that is substantially (or fully) enveloped by the source (e.g., Beaulieu et al. 2006; Hwang et al. 2018). Therefore, we begin by applying the binary-lens single-source (2L1S) interpretation to the event to explain the observed brightness variation.

3.1. Ground-based Model

We first model the light curve based on the data acquired from the ground-based observations. For our standard binary-lens model, we introduce seven nonlinear parameters (see the appendix of Jung et al. 2015 for a graphical presentation of the parameters.) This includes three single-lens parameters (t_0, u_0, $t_{\rm E}$), three parameters for the binary companion (s, q, α), and one parameter for the source radius ρ. Here, u_0 is the impact parameter (in units of $\theta_{\rm E}$), s is the companion-host projected separation (in units of $\theta_{\rm E}$), $q = M_2/M_1$ is their mass ratio, and α is their orientation angle with respect to $\boldsymbol{\mu}_{\rm rel}$. In addition, we introduce two flux parameters

$(f_S, f_B)_i$ for each data set in order to model the observed flux $f_i(t)$ as

$$f_i(t) = f_{S,i} A(t) + f_{B,i}, \quad (5)$$

where $A(t)$ is the magnification given by the model and the subscripts "S" and "B" denote the source and any blended light, respectively.

With these fitting parameters, we carry out a systematic analysis by following the procedure of Jung et al. (2015). First, we estimate initial values of $(t_0, u_0, t_E) = (8277.17, 0.28, 28.83\,\mathrm{days})$ by fitting a 1L1S curve to the data set with the anomaly excluded. We also adopt an initial value of $\rho = 0.01$ based on t_E and the source brightness estimated from the fit. We next perform a grid search over (s, q), in which (s, q) are held fixed, while $(t_0, u_0, t_E, \alpha, \rho)$ are sought based on a downhill approach. For this approach, as well as for determining the uncertainties of the parameters, we employ a Markov Chain Monte Carlo (MCMC) algorithm. For each set of fitting parameters, the lensing magnification is evaluated by inverse ray-shooting (Kayser et al. 1986; Schneider & Weiss 1987) in the anomaly region and by semianalytic approximations (Gould 2008; Pejcha & Heyrovský 2009) elsewhere. This model magnification is then used to fit the flux parameters $(f_S, f_B)_i$ that minimize the χ^2 of the observed flux $f_i(t)$.

Figure 2 displays the $\Delta\chi^2$ distribution on the $(\log s, \log q)$ space acquired from the grid search. We identify two local minima, one with $s < 1$ ("Close") and the other with $s > 1$ ("Wide"). We find that in both solutions, the lens system responsible for the weak "bump" is composed of two masses with $q \lesssim 10^{-4}$, implying that the lower-mass component is a planet. We then seed the local solutions into MCMCs and allow all fitting parameters to vary. The two standard solutions derived from this refinement process are given in Tables 1 and 2.

3.2. Microlens Parallax and Lens Orbital Motion

We now take into account the microlens parallax in order to simultaneously model the data obtained from the ground and *Spitzer*. This introduces two additional parameters $\boldsymbol{\pi}_E = (\pi_{E,N}, \pi_{E,E})$, which represent the vector microlens parallax (Gould 1992), i.e.,

$$\boldsymbol{\pi}_E = \frac{\pi_{rel}}{\theta_E} \frac{\boldsymbol{\mu}_{rel}}{\mu_{rel}}. \quad (6)$$

Then, the parallax parameters are approximately related to the offset $\Delta\boldsymbol{u} = (\Delta\beta, \Delta\tau)$ between the two light curves observed from the ground and *Spitzer*, i.e.,

$$\boldsymbol{\pi}_E = \frac{\mathrm{au}}{D_\perp}(\Delta\beta, \Delta\tau); \quad \Delta\beta = u_{0,\oplus} - u_{0,\mathrm{sat}};$$
$$\Delta\tau = \frac{t_{0,\oplus} - t_{0,\mathrm{sat}}}{t_E}, \quad (7)$$

where $D_\perp$ is the projected Earth-*Spitzer* separation and $(\Delta\beta, \Delta\tau)$ represent the components of the lens-source separation vector that are perpendicular to and parallel with the source trajectory, respectively. For single-lens events, the perpendicular offset $\Delta\beta$ generally suffers from a fourfold degeneracy

$$\Delta\beta = \pm u_{0,\oplus} - \pm u_{0,\mathrm{sat}}, \quad (8)$$

due to the rotational symmetry of the lensing magnification about the lens (Refsdal 1966; Gould 1994). These four possible solutions are usually denoted by (+, +), (−, −), (+, −), and (−, +) depending on the signs of $u_{0,\oplus}$ and $u_{0,\mathrm{sat}}$. For binary lenses, however, the fourfold degeneracy persists only if the source trajectory is almost parallel to the binary axis, i.e., $\alpha \sim 0$ (Zhu et al. 2015), and otherwise is reduced to a twofold degeneracy: (+, +) and (−, −). We therefore expect that OGLE-2018-BLG-0596 may only suffer from a twofold degeneracy, but we need a detailed analysis to draw a definitive conclusion.

To conduct a systematic analysis, we first consider additional information extracted from the ground- and space-based observations. As shown in Figure 1, the *Spitzer* data only cover the falling side of the event and do not cover the anomaly. In such a case, it is difficult to precisely constrain $\boldsymbol{\pi}_E$ from the data alone. We therefore apply a color constraint on the *Spitzer* source flux to improve the parallax measurement (Yee et al. 2015b). For this, we derive an *IHL* color–color relation using the OGLE, UKIRT, and *Spitzer* data based on the method described by Calchi Novati et al. (2015b).[42] From a model-independent regression of *I*- and *H*-band data (Gould et al. 2010), we first measure the instrumental $(I-H)$ color of the source as $(I-H)_S = 2.81 \pm 0.01$. We next construct $(I-H, I)$ and $(I-L, I)$ instrumental color–magnitude diagrams (CMDs) by cross-matching field stars within 120″ of the source. We then conduct the color–color regression on red giant stars $(15 < I < 18; 2.4 < (I-H) < 3.0)$ to confine the sample to the bulge population. From this, we find $(I-L) = 1.43\,(I-H) - 8.72$. We thereby derive $(I-L)_S = -4.70 \pm 0.02$, where the instrumental *Spitzer* magnitude is given by $L = 25 - 2.5 \log f_{S,Spitzer}$. We impose this color constraint on the model by adding a χ^2 penalty, i.e.,

$$\chi^2_{\mathrm{penalty}} = \frac{[2.5 \log(R_{\mathrm{model}}/R_{\mathrm{constraint}})]^2}{\sigma^2_{\mathrm{constraint}}}, \quad (9)$$

where R is the flux ratio between I and L bands and $\sigma_{\mathrm{constraint}}$ is the uncertainty of $(I-L)_S$.

Space-based observations can provide an opportunity not only to measure the microlens parallax but also to constrain the orbital motion of the binary lens (Han et al. 2016). As discussed by Batista et al. (2011), the annual microlens parallax (due to Earth's orbital motion) can be partially degenerate with the lens orbital motion, and so the microlens parallax measured from a single accelerating frame can absorb the lens orbital motion. By contrast, the space-based microlens parallax does not suffer from this degeneracy because it is determined from the feature of the light curves from two different observatories. This enables one to break such degeneracy and detect the lens orbital motion in the ground-based light curve. Therefore, we also take into account the lens orbital effect. To account for this effect, we introduce two linearized parameters $(ds/dt, d\alpha/dt)$, which represent the relative velocity of the lens components projected onto the plane of the sky (Dominik 1998; Jung et al. 2013).

We now model the light curve with a set of parameters $(t_0, u_0, t_E, s, q, \alpha, \rho, \pi_{E,N}, \pi_{E,E}, ds/dt, d\alpha/dt)$ and the color constraint described above. For each of the Close and Wide configurations obtained from the ground data sets, we first conduct a grid search for the parameters $(\pi_{E,N}, \pi_{E,E})$ in order to check the four possibilities of the $\boldsymbol{\pi}_E$ measurement. We then rerun the MCMC process with various starting points identified in the $(\pi_{E,N}, \pi_{E,E})$ space. From this, we find that in both configurations, all MCMC chains converged to two points (see

[42] We note that the *Spitzer* bandpass is centered at 3.6 μm, which we designate as the *L* band.

Table 1
Lensing Parameters for Close Solutions

Parameters	Standard	Parallax		Orbit+Parallax	
		(+, +)	(−, −)	(+, +)	(−, −)
$\chi^2_{\rm tot}$/dof	25959.6/26562	25901.6/26596	25906.6/26596	25895.4/26594	25897.3/26594
t_0 (HJD′)	8277.16 ± 0.010	8277.14 ± 0.010	8277.14 ± 0.010	8277.14 ± 0.015	8277.14 ± 0.015
u_0	0.285 ± 0.002	0.285 ± 0.004	−0.284 ± 0.004	0.284 ± 0.006	−0.282 ± 0.006
$t_{\rm E}$ (days)	28.881 ± 0.109	28.924 ± 0.110	29.038 ± 0.109	29.003 ± 0.110	29.170 ± 0.116
s	0.566 ± 0.003	0.564 ± 0.005	0.565 ± 0.005	0.512 ± 0.017	0.499 ± 0.018
q (10^{-4})	1.203 ± 0.089	1.327 ± 0.105	1.313 ± 0.106	1.827 ± 0.132	1.879 ± 0.133
α (rad)	6.072 ± 0.009	6.076 ± 0.011	−6.071 ± 0.011	6.022 ± 0.011	−6.025 ± 0.014
ρ_* (10^{-2})	1.120 ± 0.042	1.139 ± 0.043	1.137 ± 0.042	1.347 ± 0.049	1.362 ± 0.050
$\pi_{{\rm E},N}$	⋯	−0.041 ± 0.023	0.043 ± 0.022	−0.023 ± 0.022	0.033 ± 0.026
$\pi_{{\rm E},E}$	⋯	0.177 ± 0.010	0.179 ± 0.010	0.178 ± 0.010	0.177 ± 0.010
ds/dt (yr^{-1})	⋯	⋯	⋯	−0.580 ± 0.045	−0.734 ± 0.031
$d\alpha/dt$ (yr^{-1})	⋯	⋯	⋯	−0.637 ± 0.101	0.566 ± 0.135
$f_{\rm S}$	1.956 ± 0.002	1.955 ± 0.002	1.945 ± 0.002	1.945 ± 0.002	1.930 ± 0.002
$f_{\rm B}$	−0.044 ± 0.003	−0.043 ± 0.003	−0.032 ± 0.003	−0.032 ± 0.003	−0.017 ± 0.003
$\chi^2_{\rm ground}$	25959.6	25867.4	25871.6	25860.9	25861.8
$\chi^2_{Spitzer}$	⋯	34.1	34.9	34.5	35.1
$\chi^2_{\rm penalty}$	⋯	0.11	0.14	0.0079	0.43

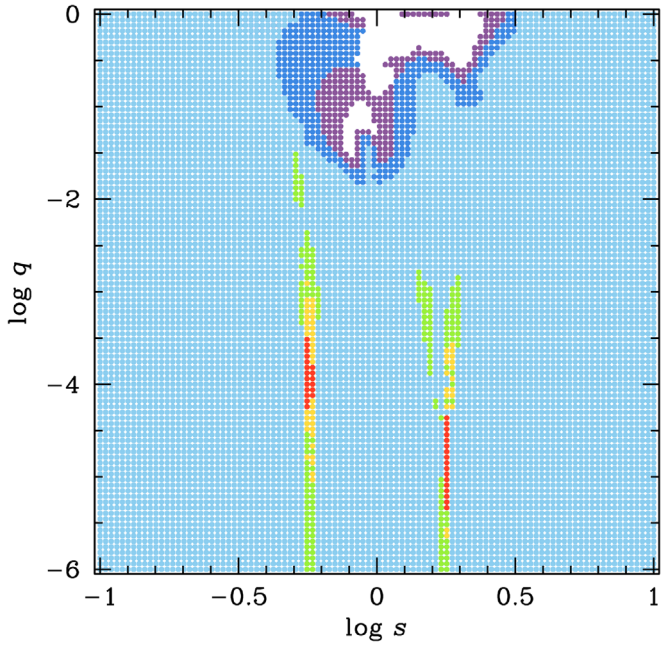

Figure 2. $\Delta\chi^2$ map in (log s, log q) space drawn from the grid search. The space is equally divided on a (100 × 100) grid with ranges of $-1 < \log s < 1$ and $-6 < \log q < 0$, respectively. The contour is color coded by (red, yellow, green, light blue, blue, and purple) for $\Delta\chi^2 < [(1\,n)^2, (2\,n)^2, (3\,n)^2, (4\,n)^2, (5\,n)^2$, and $(6\,n)^2]$, where $n = 20$.

the second and third columns in Tables 1 and 2). That is, they do not suffer from the degeneracy between the pair of [(+, +), (+, −)] or [(−, −), (−, +)], and only suffer from the degeneracy between the pair of [(+, +), (−, −)]. The latter degeneracy is induced by the mirror symmetry of source trajectories relative to the binary axis, i.e., the "ecliptic degeneracy" (Jiang et al. 2004; Skowron et al. 2011). Finally, we further investigate the solutions by including the lens orbital effects.

In Tables 1 and 2, we present the four solutions, i.e., [(+, +), (−, −)] × (Close, Wide), solutions. The corresponding caustic geometries are shown in Figure 3. We find that in each solution, the source star fully envelops a planetary caustic that is located far from the host. In the Close configuration, the anomaly is generated by the envelopment of one of the triangular caustics, while in the Wide configuration it is generated by the envelopment of the quadrilateral caustic (e.g., Hwang et al. 2019). The most important difference between the two sets of solutions is in the mass ratio q, which is almost 10 times smaller in the Wide solutions.

3.3. Additional Test for Microlens Parallax

We find that the χ^2 difference of the ground data sets between the standard and best-fit $(+, +)_{\rm Close}$ solution is $\Delta\chi^2 \sim 99$ (see Table 1). This suggests that the microlens parallax is partially constrained by the annual microlens parallax effect. To better understand this, we additionally model the ground-based light curve with the lens orbital effect and the annual parallax effect ("orbit+AP").

However, we find the possibility that the χ^2 improvement is caused by systematics of the data. From the cumulative distribution of $\Delta\chi^2 = \chi^2_{\rm standard} - \chi^2_{\rm orbit+AP}$ as a function of time, we find that there is a long-term inconsistent trend between KMTNet+MOA and the other data sets (see Figure 4). That is, most of the improvement comes from the KMTNet +MOA data, while the improvement from the other data is very minor. This discrepancy implies that these two data sets may not be stable enough to precisely explore the parameter space (e.g., Han et al. 2018). From this, one might further conjecture that our $\pi_{\rm E}$ measurements are affected by false-positive effects caused by the systematics. We therefore step back and carry out a series of tests to verify our solutions.

First, we fit for the geometric parameters using only the *Spitzer* data and the color constraint. That is, we exclude the ground observations in order to identify all possible combinations of ($\pi_{{\rm E},N}$, $\pi_{{\rm E},E}$) that are consistent with the space observations alone. In this modeling, the lensing geometry seen from the ground is set by imposing Gaussian constraints on the fitting parameters (t_0, u_0, $t_{\rm E}$, $f_{\rm S,OGLE}$, $f_{\rm B,OGLE}$) based on the ground-based solution derived in Section 3.1. Next, we include all data sets except for KMTNet and MOA, for which

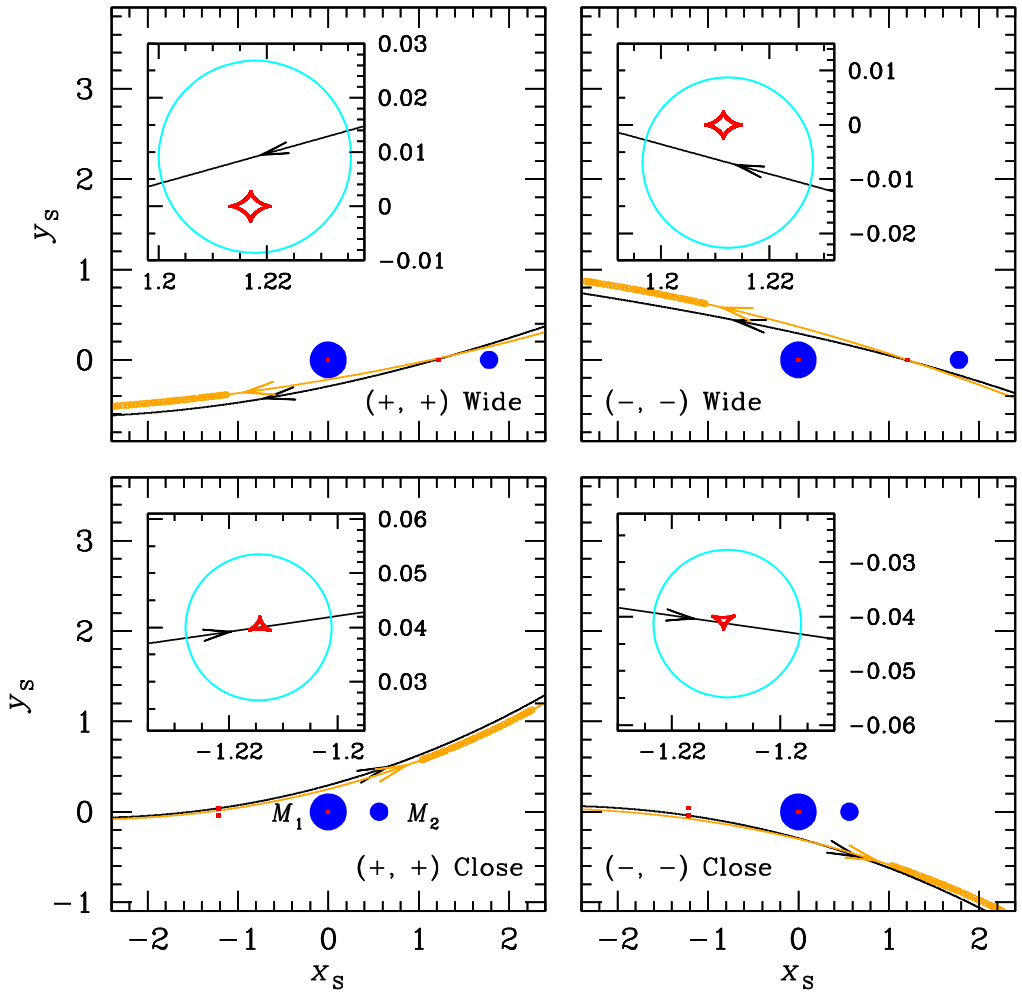

Figure 3. Caustic geometries of the four solutions of OGLE-2018-BLG-0596. In each panel, the orange curve is the *Spitzer*-viewed source trajectory, while the black curve is the Earth-viewed source trajectory. The orange circles are the source positions at the times of *Spitzer* observation. These are not shown to scale in order to avoid clutter. The red closed curves are the caustics, and the two dark blue dots are the binary-lens components. The inset shows the enlarged view of the small planetary caustic at the time of the source's caustic envelopment. The cyan circle represents the source radius ρ of the best-fit solution (see Tables 1 and 2).

Table 2
Lensing Parameters for Wide Solutions

Parameters	Standard	Parallax		Orbit+Parallax	
		(+, +)	(−, −)	(+, +)	(−, −)
$\chi^2_{\rm tot}$/dof	26009.5/26562	25915.7/26596	25926.1/26596	25912.2/26594	25924.0/26594
t_0 (HJD′)	8277.16 ± 0.010	8277.13 ± 0.011	8277.14 ± 0.011	8277.13 ± 0.015	8277.13 ± 0.014
u_0	0.286 ± 0.002	0.284 ± 0.004	−0.286 ± 0.004	0.285 ± 0.006	−0.285 ± 0.005
$t_{\rm E}$ (days)	28.833 ± 0.107	28.974 ± 0.110	28.870 ± 0.105	28.889 ± 0.107	28.894 ± 0.105
s	1.769 ± 0.004	1.773 ± 0.006	1.775 ± 0.006	1.811 ± 0.015	1.788 ± 0.016
q (10^{-4})	0.160 ± 0.015	0.187 ± 0.015	0.181 ± 0.014	0.244 ± 0.027	0.188 ± 0.019
α (rad)	2.897 ± 0.011	2.899 ± 0.018	−2.901 ± 0.015	2.929 ± 0.018	−2.921 ± 0.016
ρ_* (10^{-2})	1.495 ± 0.066	1.587 ± 0.074	1.591 ± 0.058	1.772 ± 0.078	1.572 ± 0.059
$\pi_{{\rm E},N}$	⋯	−0.061 ± 0.025	−0.071 ± 0.024	−0.075 ± 0.026	−0.078 ± 0.032
$\pi_{{\rm E},E}$	⋯	0.191 ± 0.010	0.157 ± 0.010	0.193 ± 0.011	0.159 ± 0.011
ds/dt (yr^{-1})	⋯	⋯	⋯	0.371 ± 0.048	0.151 ± 0.036
$d\alpha/dt$ (yr^{-1})	⋯	⋯	⋯	0.355 ± 0.089	−0.225 ± 0.091
$f_{\rm S}$	1.961 ± 0.002	1.949 ± 0.002	1.961 ± 0.002	1.959 ± 0.002	1.958 ± 0.002
$f_{\rm B}$	−0.048 ± 0.003	−0.035 ± 0.003	−0.047 ± 0.003	−0.045 ± 0.003	−0.045 ± 0.003
$\chi^2_{\rm ground}$	26009.5	25881.5	25890.3	25878.3	25887.5
$\chi^2_{\textit{Spitzer}}$	⋯	34.1	35.6	33.9	35.6
$\chi^2_{\rm penalty}$	⋯	0.12	0.16	0.0019	0.94

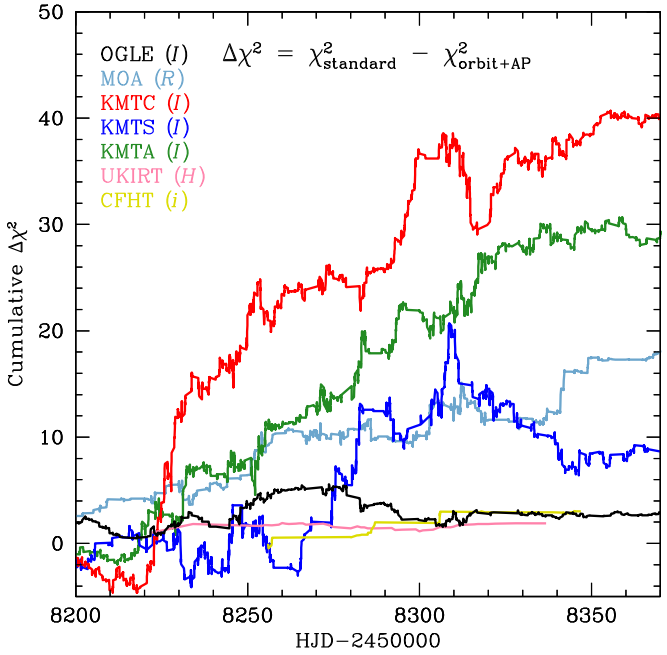

Figure 4. Cumulative distribution of $\Delta\chi^2$ between the standard and the "orbit +AP" solution derived from the ground-based observations. Note that the diagram is constructed using the best-fit model from the $(+, +)_{\rm Close}$ caustic topology.

we use only partial data sets. While the parallax parameters are measured from the overall shape of the light curve, the binary parameters are measured from the anomaly. For this event, the overall shape is well characterized by the other data sets, but their coverage near the anomaly is very poor. To account for the anomaly as well as to remove any spurious parallax effects originating from possible systematics, we therefore use only the data near the anomaly region (specifically $8235 < {\rm HJD}' < 8250$) for KMTNet and MOA. With these modified data sets, we then run full MCMC chains incorporating all models obtained from the first step.

From this test, we find that all MCMC chains converged to two points for both the Close and Wide configurations. In addition, the locations of these two points in each configuration are nearly identical to those derived from the full data sets, indicating that the measured parallaxes are consistent with each other. This consistency can be seen in Figure 5, where we show the $\Delta\chi^2$ maps in the $(\pi_{{\rm E},N}, \pi_{{\rm E},E})$ plane obtained from the test. We note that the cross mark in each panel represents the location of $\boldsymbol{\pi}_{\rm E}$ listed in Tables 1 and 2, i.e., the four solutions. From this figure, one also finds that only the $(+, +)$ and $(-, -)$ models are permitted by the modified ground-based data sets. Therefore, we conclude that our four solutions are not significantly affected by systematics.

3.4. Close/Wide Degeneracy

The χ^2 difference between the $(+, +)_{\rm Close}$ and $(+, +)_{\rm Wide}$ solution is $\Delta\chi^2 \sim 17$.[43] Mathematically, this implies that the probability of $(+, +)_{\rm Wide}$ solution relative to the $(+, +)_{\rm Close}$ solution is lowered by $P_{\rm lc} = e^{-\Delta\chi^2/2} \sim 2 \times 10^{-4}$. However, this relative fit probability depends on the assumption that all data have uncorrelated errors. Unfortunately, such conditions are generally not satisfied for crowded field photometry. Hence, it is difficult to entirely reject the $(+, +)_{\rm Wide}$ solution from the measured $\Delta\chi^2$ alone.

Nevertheless, we can better understand the χ^2 difference by inspecting the cumulative distribution of $\Delta\chi^2 = \chi^2_{(+,+)_{\rm Wide}} - \chi^2_{(+,+)_{\rm Close}}$ (see Figure 6). From this, we find that most of the difference comes from the rising part of the anomaly (${\rm HJD}' \sim 8241$), where the $(+, +)_{\rm Wide}$ solution provides a relatively poor fit to the data. In this region, the $(+, +)_{\rm Wide}$ model curve is on average located 0.01 mag above that of the $(+, +)_{\rm Close}$ solution due to the difference in the lensing magnification field. For the Close configuration, the source passes over the negative planet-host axis during the few days immediately prior to the planetary-caustic anomaly (see Figure 3). Generically, this axis is characterized by a trough (e.g., Gaudi 2012). By contrast, the Wide configuration has no such trough. Moreover, the short-term deviation that favors the Close solution cannot be ascribed to the type of long-term systematics discussed above. Therefore, we consider that the Wide solutions are disfavored. We will further discuss this preference of the data in Section 4.2.

3.5. Single-lens Binary-source Model

As discussed by Gaudi (1998), short-term anomalies can also be produced by a binary source, i.e., 1L2S event. In particular, if the binary source (denoted as "S1" and "S2") has a large flux ratio $q_F = f_{\rm S2}/f_{\rm S1}$ and the second source passes very close to the lens, the resulting light curve can take a similar form to that of a 2L1S planetary event. We therefore search for 1L2S solutions based on the method of Jung et al. (2017). In this search, we simultaneously consider the parallax effect, finite-source effect, and orbital motion of the binary source (the xallarap effect). We find that the best-fit 1L2S solution is disfavored by $\Delta\chi^2 \sim 87$. To check the result, we also draw the cumulative $\Delta\chi^2$ distribution of the 1L2S solution relative to the best-fit 2L1S solution. As shown in Figure 6, we find that most of the χ^2 difference comes from the short-lived anomaly region ($8240 < {\rm HJD}' < 8245$), in which the 1L2S solution continuously fails to fit the observed light curve. Hence, we exclude the 1L2S solution.

4. Lens Parameters

The lens total mass M and distance $D_{\rm L}$ can be determined from $\pi_{\rm E}$ and $\theta_{\rm E}$ (Equation (3)). These enable us to derive the individual masses of the binary lens and their projected separation $a_\perp = sD_{\rm L}\theta_{\rm E}$ from the measured mass ratio q and separation s. In addition, if the source proper motion $\boldsymbol{\mu}_{\rm S}$ is measured, we can derive the lens proper motion $\boldsymbol{\mu}_{\rm L}$ from the relative lens-source proper motion $\boldsymbol{\mu}_{\rm rel}$ (Equation (4)). Then, the lens proper motion can be used to precisely constrain the lens physical properties. For the event OGLE-2018-BLG-0596, the proper motion of the microlensed source is independently measured from the *Gaia* observation (the *Gaia* Data Release 2 ID is 4056540540298891520). As will be discussed below, this measurement provides us with an additional opportunity to investigate the degeneracy between our four solutions.

The microlens parallax is measured from the model, while the Einstein radius can be measured from $\theta_{\rm E} = \theta_*/\rho$. Therefore, we first need to determine the angular source radius θ_*.

[43] We note that the best-fit solution in each configuration is the $(+, +)_{\rm Close}$ and $(+, +)_{\rm Wide}$ solution, and so we consider these two solutions as the representatives.

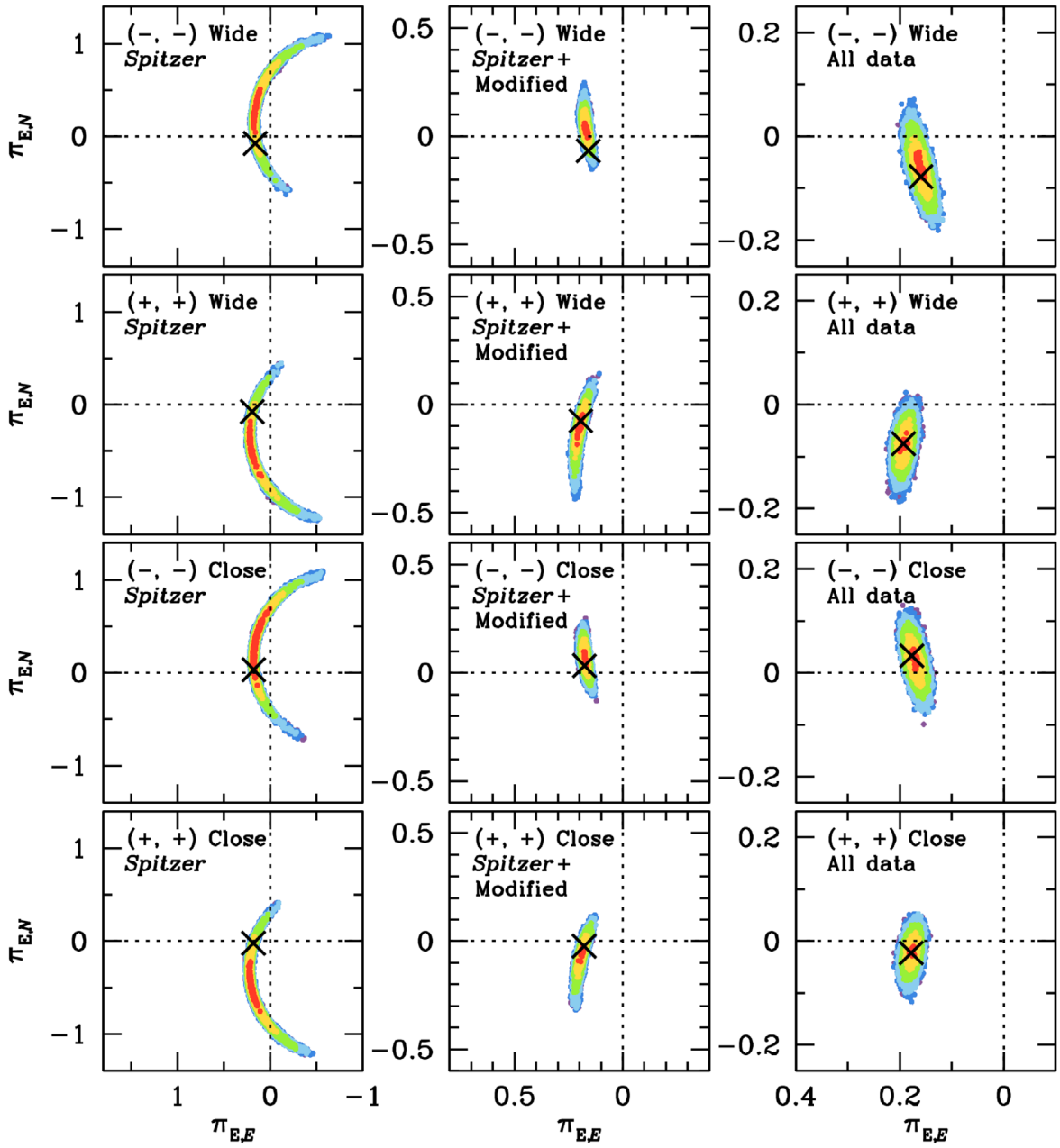

Figure 5. χ^2 as a function of microlens parallax for different data sets. The left, middle, and right four panels show the derived $\Delta\chi^2$ maps in the ($\pi_{E,N}$, $\pi_{E,E}$) plane based on the *Spitzer* data, *Spitzer*+modified ground data, and all data sets, respectively. In each panel, the black cross marks the location of $\boldsymbol{\pi}_E$ listed in Tables 1 and 2. Except that here $n = 1$, the color coding is the same as in Figure 2. Note the different scales in the three columns.

4.1. Angular Source Radius

We evaluate θ_* using the method of Yoo et al. (2004). Based on the KMTC star catalog constructed by the pyDIA reduction, we first estimate the instrumental source color $(V-I)_S = 2.65 \pm 0.01$ and magnitude $I_S = 17.19 \pm 0.01$ from regression and the model, respectively. We next measure the centroid of the giant clump (GC) as $(V-I,\ I)_{GC} = (2.57 \pm 0.02,\ 16.29 \pm 0.02)$. Figure 7 displays the locations of the source and GC in the KMTC CMD. We then compare this centroid to the calibrated centroid of $(V-I,\ I)_{0,GC} = (1.06 \pm 0.07,\ 14.40 \pm 0.09)$ obtained from Bensby et al. (2013) and Nataf et al. (2013), respectively. This yields an offset $\Delta(V-I,\ I) = (1.51 \pm 0.07,\ 1.89 \pm 0.09)$. Using this offset, we estimate the dereddened source position as

$$(V-I,\ I)_{0,S} = (V-I,\ I)_S - \Delta(V-I,\ I) = (1.14 \pm 0.07,\ 15.30 \pm 0.09). \quad (10)$$

We then apply $(V-I)_{0,S}$ to the *VIK* relation of Bessell & Brett (1988) and derive $(V-K)_{0,S} = 2.63 \pm 0.07$. Finally, we estimate θ_* from the $(V-K)_{0,S} - \theta_*$ relation of Kervella et al. (2004), i.e.,

$$\theta_* = 4.46 \pm 0.38\ \mu\text{as}, \quad (11)$$

where the error is primarily due to the uncertainty of the GC position and color/surface-brightness conversion. The derived source star properties are listed in Table 3.

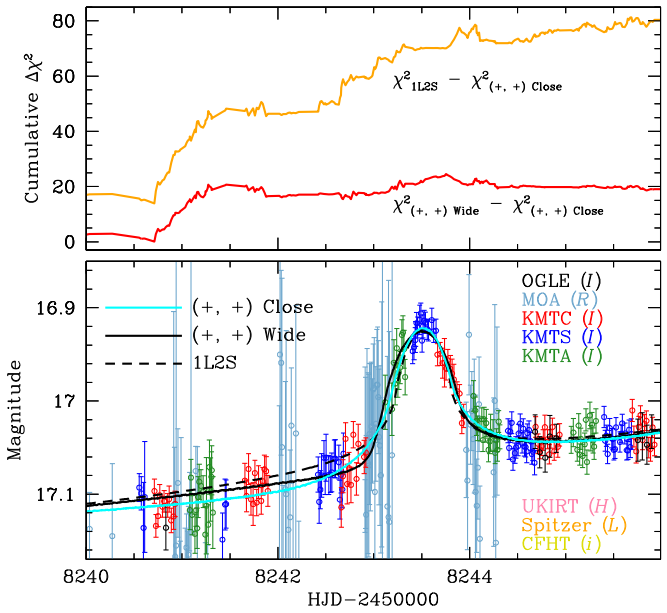

Figure 6. Cumulative distributions of $\Delta\chi^2$ in the anomaly region. In the upper panel, the red and orange curves represent the χ^2 differences between the $(+, +)_{\rm Wide}$ and $(+, +)_{\rm Close}$ solution and between the 1L2S and $(+, +)_{\rm Close}$ solution, respectively. In the lower panel, the cyan, black solid, and black dashed curves plotted over the data are the model curves based on the $(+, +)_{\rm Close}$, $(+, +)_{\rm Wide}$, and 1L2S solution, respectively.

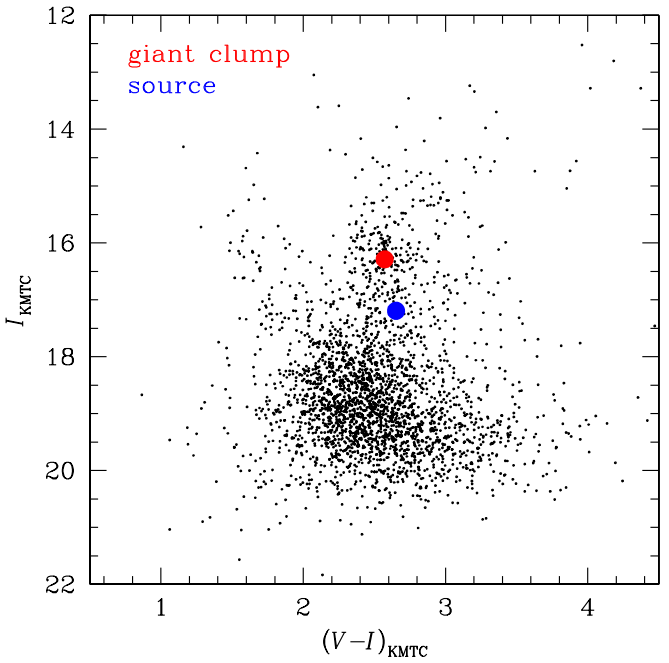

Figure 7. Instrumental color–magnitude diagram of stars around OGLE-2018-BLG-0596 (within 120″) based on the KMTC star catalog. The red and blue dots indicate the positions of the giant clump centroid (GC) and the microlensed source, respectively.

4.2. Source Proper Motion and Galactic Prior

The source star of OGLE-2018-BLG-0596 is bright (as derived above), and the blend flux associated with the lensing phenomenon is negligible (see Tables 1 and 2). In this case, the proper motion measured by *Gaia* can be attributed to that of the source. Then, we can use this measurement to estimate the relative probability of our four solutions by comparing the lens projected velocity (from the model) with that expected from the known Galactic velocity distribution.

For this comparison, we first estimate the lens projected velocity using the four MCMC chains summarized in Tables 1 and 2. For each chain, we first derive the angular Einstein radius $\theta_{\rm E}$ based on the measured θ_*. We next estimate the relative lens-source proper motion in the geocentric frame (Equation (3)), and transform it to the heliocentric frame, i.e.,

$$\boldsymbol{\mu}_{\rm rel,hel} = \boldsymbol{\mu}_{\rm rel} + \boldsymbol{\nu}_{\oplus,\perp}\frac{\pi_{\rm rel}}{\rm au}, \quad (12)$$

where $\boldsymbol{\nu}_{\oplus,\perp} = (\nu_{\oplus,N}, \nu_{\oplus,E}) = (0.47, 28.61)$ km s^{-1} is the projected velocity of Earth at t_0 (Gould 2004). The lens proper motion in the heliocentric frame is then given by

$$\boldsymbol{\mu}_{\rm L,hel} = \boldsymbol{\mu}_{\rm rel,hel} + \boldsymbol{\mu}_{\rm G}, \quad (13)$$

where $\boldsymbol{\mu}_{\rm G}(N, E) = (-5.26 \pm 0.55, -4.92 \pm 0.66)$ mas yr^{-1} is the source proper motion measured from *Gaia* (Luri et al. 2018). We then estimate the lens proper motion $\boldsymbol{\mu}_{\rm L,gal}$ in Galactic coordinates with the coordinate transform of Bachelet et al. (2018). We finally derive the lens projected velocity relative to the local standard of rest (LSR) by

$$\boldsymbol{\nu}_{\rm L} = \boldsymbol{\mu}_{\rm L,gal} D_{\rm L} + \boldsymbol{\nu}_{\odot,\rm pec}, \quad (14)$$

Table 3
Derived Properties for Source Star

Parameter	Units	Value
$I_{\rm S}$	[mag]	17.19 ± 0.01
$(V-I)_{\rm S}$		2.65 ± 0.01
$I_{0,\rm S}$	[mag]	15.30 ± 0.09
$(V-I)_{0,\rm S}$		1.14 ± 0.07
$(V-K)_{0,\rm S}$		2.63 ± 0.07
θ_*	[μas]	4.46 ± 0.38

Note.
[a] See Section 4.1 for details.

where $\boldsymbol{\nu}_{\odot,\rm pec} = (\nu_{\odot,W}, \nu_{\odot,V}) = (7, 12)$ km s^{-1} (Schönrich et al. 2010) is the peculiar motion of the Sun relative to the LSR.[44] In Figure 8, we show the distributions of $\boldsymbol{\nu}_{\rm L}$ obtained from the four MCMC chains. We note that the W and V axis are defined in Cartesian coordinates so that the components point in the direction of the north Galactic pole and the Galactic rotation, respectively.

Next, we construct the Galactic velocity distribution in the LSR frame based on the model of Robin et al. (2003). Because the lens distance is $D_{\rm L} \sim 6$ kpc (as derived below), it is expected that the lens is located in the Galactic disk or outer bulge. Therefore, we separately consider the bulge, thin disk, and thick disk distributions. We use $\bar{\nu}_{{\rm gal},W} = (\bar{\nu}_{{\rm bulge},W}, \bar{\nu}_{{\rm thin},W}, \bar{\nu}_{{\rm thick},W}) = (0, 0, 0)$ km s^{-1} and $\bar{\sigma}_{{\rm gal},W} = (\bar{\sigma}_{{\rm bulge},W}, \bar{\sigma}_{{\rm thin},W}, \bar{\sigma}_{{\rm thick},W}) = (100, 20, 42)$ km s^{-1} for the W-direction and $\bar{\nu}_{{\rm gal},V} = (\bar{\sigma}_{{\rm bulge},V}$,

[44] To estimate $D_{\rm L}$, we generate a large number of $D_{\rm S}$ based on a distance distribution drawn from the density profile of the Galactic bulge (e.g., Jung et al. 2018b).

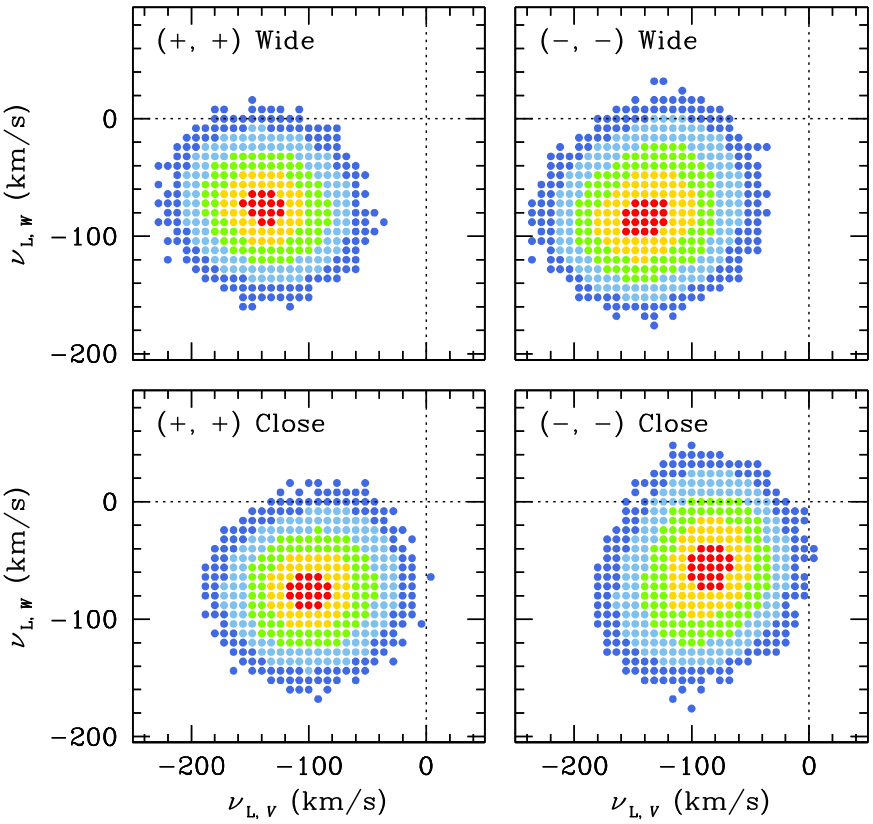

Figure 8. Distributions of lens projected velocities $\boldsymbol{\nu}_{\rm L}$ estimated from the four solutions. The color notation is the same as in Figure 5. Note that the reference frame is the local standard of rest (LSR).

$\bar{\sigma}_{{\rm thin},V}$, $\bar{\sigma}_{{\rm thick},V}$) = (−220, 0, 0) km s^{-1} and $\bar{\sigma}_{{\rm gal},V}$ = ($\bar{\sigma}_{{\rm bulge},V}$, $\bar{\sigma}_{{\rm thin},V}$, $\bar{\sigma}_{{\rm thick},V}$) = (115, 30, 51) km s^{-1} for the V-direction with the asymmetric drift of ($\nu_{\rm ad,bulge}$, $\nu_{\rm ad,thin}$, $\nu_{\rm ad,thick}$) = (0, 0, −53) km s^{-1}.

In each solution, we separately apply three model distributions to the kth chain link and derive a probability that the lens has the projected velocity expected from the model distribution, i.e.,

$$P_{{\rm gal},k} = \left[\frac{e^{-(\nu_{{\rm L},W}-\nu_{{\rm gal},W})^2/2\bar{\sigma}^2_{{\rm gal},W}} e^{-(\nu_{{\rm L},V}-\nu_{{\rm gal},V})^2/2\bar{\sigma}^2_{{\rm gal},V}}}{\bar{\sigma}_{{\rm gal},W}\bar{\sigma}_{{\rm gal},V}}\right] \times \rho_{\rm d,\ gal}(D_{\rm L})\rho_{\rm d,\ bulge}(D_{\rm S}), \quad (15)$$

where $\boldsymbol{\nu}_{\rm gal} = \bar{\boldsymbol{\nu}}_{\rm gal} + \boldsymbol{\nu}_{\rm ad}$ and $\rho_{\rm d,gal}$ = ($\rho_{\rm d,bulge}$, $\rho_{\rm d,thin}$, $\rho_{\rm d,thick}$) is the Galactic density profile presented in Jung et al. (2018b). We then estimate the three probabilities ($P_{\rm bulge}$, $P_{\rm thin}$, $P_{\rm thick}$) by $P_{\rm gal} = \Sigma P_{{\rm gal},k}$, and find the total probability $P_{\rm tot,gal}$ by combining these three probabilities, i.e., $P_{\rm tot,gal} = P_{\rm bulge} + P_{\rm thin} + P_{\rm thick}$. Finally, we derive the net relative probability $P_{\rm net}$ by multiplying the fit probability $P_{\rm lc} = e^{-(\chi^2-\chi^2_{\rm best})/2}$ by $P_{\rm tot,gal}$.

The results are listed in Table 4. We find that in both the Close and Wide configurations, the lens system favors the bulge populations. This is mainly because the direction of lens projected velocity $\boldsymbol{\nu}_{\rm L}$ is opposite with respect to the LSR and its magnitude is relatively high compared to the rotational velocity $v_{\rm rot}$ =220 km s^{-1} (see Figure 8). From Table 4, we also find that the Galactic-model probabilities $P_{\rm tot,gal}$ are comparable to each other and do not lend significant weight to either solution, implying that the preference for the Close solutions discussed in Section 3.4 is not significantly affected by the Galactic prior. Therefore, we can consider that from the balance of evidence $P_{\rm net}$, the Close configuration is strongly favored although the Wide configuration cannot be completely ruled out.

Table 4
Relative Probabilities

Parameters	Close		Wide	
	(+, +)	(−, −)	(+, +)	(−, −)
$P_{\rm lc}$	1.0	0.37	2.04×10^{-4}	5.04×10^{-7}
$P_{\rm thin}$	0.24	8.52	1.21×10^{-2}	4.08×10^{-2}
$P_{\rm thick}$	14.11	40.60	8.14	7.39
$P_{\rm bulge}$	78.46	101.19	160.04	185.63
$P_{\rm tot,gal}$	92.81	150.31	168.19	193.06
$P_{\rm net}$	92.81	55.61	3.43×10^{-2}	9.73×10^{-5}

4.3. Physical Parameters

For each solution, we now estimate the physical parameters a_j by imposing the Galactic prior. In the kth set of MCMC parameters, we evaluate the physical parameters $a_{j,k}$ with the measured θ_* and weight them by the probability $P_{{\rm gal},k}$. We then derive the mean and 68% uncertainty range of a_j using all weighted $a_{j,k}$.

The results are listed in Table 5, which includes the lens physical properties (M_1, M_2, $a_\perp$) and the event's phase-space coordinates ($D_{\rm L}$, $D_{\rm S}$, $\mu_{\rm rel}$, $\boldsymbol{\mu}_{\rm rel,hel}$, ϕ, $\boldsymbol{\mu}_{\rm L,hel}$, $\boldsymbol{\nu}_{\rm L}$). Here, ϕ is the

Table 5
Physical Parameters

Parameters	$(+, +)_{\rm Close}$	$(-, -)_{\rm Close}$	$(+, +)_{\rm Wide}$	$(-, -)_{\rm Wide}$
$\theta_{\rm E}$ (mas)	0.336 ± 0.034	0.324 ± 0.033	0.256 ± 0.027	0.276 ± 0.028
M_1 ($M_\odot$)	0.231 ± 0.028	0.229 ± 0.031	0.154 ± 0.019	0.196 ± 0.021
M_2 ($M_\oplus$)	13.93 ± 1.56	14.69 ± 1.72	1.19 ± 0.16	1.30 ± 0.16
$a_\perp$ (au)	0.97 ± 0.13	0.92 ± 0.14	2.77 ± 0.37	3.02 ± 0.39
$D_{\rm L}$ (kpc)	5.65 ± 0.75	5.65 ± 0.80	5.95 ± 0.77	6.11 ± 0.79
$D_{\rm S}$ (kpc)	8.58 ± 1.42	8.38 ± 1.47	8.69 ± 1.35	8.67 ± 1.33
$\mu_{\rm rel}$ (mas yr^{-1})	4.22 ± 0.42	4.07 ± 0.41	3.24 ± 0.33	3.49 ± 0.35
$\mu_{{\rm rel,hel},N}$ (mas yr^{-1})	-0.44 ± 0.50	0.64 ± 0.57	-1.13 ± 0.36	-1.14 ± 0.65
$\mu_{{\rm rel,hel},E}$ (mas yr^{-1})	4.53 ± 0.46	3.98 ± 0.43	3.33 ± 0.36	3.24 ± 0.33
ϕ (deg) (E of N)	95.5 ± 10.9	81.3 ± 10.9	108.7 ± 11.8	107.4 ± 14.3
$\mu_{{\rm L,hel},N}$ (mas yr^{-1})	-5.67 ± 0.79	-4.57 ± 0.80	-6.37 ± 0.76	-6.37 ± 0.94
$\mu_{{\rm L,hel},E}$ (mas yr^{-1})	-0.45 ± 0.41	-0.66 ± 0.44	-1.63 ± 0.44	-1.44 ± 0.41
$v_{{\rm L},W}$ (km s^{-1})	-98.8 ± 18.7	-73.6 ± 22.2	-97.1 ± 16.7	-103.5 ± 20.4
$v_{{\rm L},V}$ (km s^{-1})	-97.4 ± 20.1	-82.5 ± 18.6	-141.3 ± 22.8	-141.1 ± 24.7
$({\rm KE/PE})_\perp$ (10^{-2})	8.67 ± 2.86	10.06 ± 3.22	50.78 ± 21.92	11.91 ± 8.19

orientation angle of $\boldsymbol{\mu}_{\rm rel,hel}$ as measured north through east. To investigate the physical validity of these measurements, we also show the ratio of the projected kinetic to potential energy (Dong et al. 2009), i.e., $({\rm KE/PE})_\perp$. For all four solutions, the low values of $\mu_{\rm rel}$ and the large values of $D_{\rm L}$ favor the bulge lenses as predicted from the Galactic prior. However, the estimated lens masses for the Close and Wide configuration differ from each other due primarily to the difference in mass ratios q between the two configurations, but also, to a much smaller degree, because of the difference in the normalized source radii ρ.

The most favored $(+, +)_{\rm Close}$ solution suggests that the host is a mid M-dwarf star with $M_1 = 0.23 \pm 0.03\ M_\odot$, and that the companion is a planet with $M_2 = 13.93 \pm 1.56\ M_\oplus$. The projected planet-host separation is $a_\perp = 0.97 \pm 0.13$ au. Hence, this interpretation indicates that the planet is a cold Uranus lying projected outside the snow-line distance, i.e., $a_{sl} = 2.7(M_1/M_\odot) \sim 0.62$ au. On the other hand, the $(+, +)_{\rm Wide}$ solution corresponds to an Earth-mass planet ($M_2 = 1.19 \pm 0.16\ M_\oplus$) orbiting a late M-dwarf ($M_2 = 0.15 \pm 0.02\ M_\odot$). This planet is colder because the projected separation ($a_\perp = 2.77 \pm 0.37$ au) is about 7 times larger than the snow line.

5. Discussion

We have analyzed the microlensing event OGLE-2018-BLG-0596, which was simultaneously observed from the ground and *Spitzer*. The planetary signal in the light curve was densely covered by the data from the KMTNet survey, from which the normalized source radius was precisely measured. The *Spitzer* observations allowed us to measure the microlens parallax through the space-based microlens parallax effect. Combined with the source proper motion from *Gaia*, these measurements made it possible to precisely constrain the lens physical properties.

Analysis of the event yields four degenerate solutions originating from two different caustic topologies, i.e., $(\pm, \pm)_{\rm Close}$ and $(\pm, \pm)_{\rm Wide}$ solutions. This Close/Wide degeneracy is generated by the bright source that fully envelops either the minor-image planetary caustic (Close) or the major-image planetary caustic (Wide), i.e., a "Hollywood" degeneracy. As pointed out by Hwang et al. (2019), the Hollywood degeneracy in principle can be resolved because in Close solutions the source passes over the minor-image perturbation region, thereby causing a "dip" in the light curve near the planetary caustic. In the present case, however, the "dip" is relatively weak compared to photometric errors. Hence, the degeneracy is only resolved by $\Delta\chi^2 \sim 17$. This χ^2 difference is large enough to strongly favor the Close solutions but not enough to completely rule out the Wide solutions.

Nevertheless, the degeneracy may be decisively resolved by adaptive optics (AO) follow-up after waiting a time for the position of the lens and the microlensed source to separate. This is because the three reasonably competitive solutions [$(+, +)_{\rm Close}$, $(-, -)_{\rm Close}$, $(+, +)_{\rm Wide}$] have different heliocentric motion directions $\phi = (96 \pm 11,\ 81 \pm 11,\ 109 \pm 12)$ deg. For example, if the observed value is $\phi_{\rm AO} = 80°$, this will strongly favor the Close solutions because it is inconsistent with that of the Wide solution. If the value is $\phi_{\rm AO} = 90°$, then this would marginally disfavor the Wide solution. However, given the strong χ^2 preference for the Close solutions, this would still clearly resolve the degeneracy.

The best-fit $(+, +)_{\rm Close}$ solution has the planet-host mass ratio of $q = 1.8 \times 10^{-4}$, which is just larger than the peak in the mass ratio distribution of Jung et al. (2019a) that suggests a pile-up of Neptune-mass planets. However, even though the mass ratio is near the middle of a predicted "gap" between Neptune- and Jupiter-mass planets for solar-mass hosts, the derived physical solution has an ice-giant planet with $M_{\rm p} = 13.93 \pm 1.56\ M_\oplus$, very similar to Uranus in our solar system. This is because the lens host is a mid M-dwarf whose mass is much smaller than the solar mass, i.e., $M_{\rm h} = 0.23 \pm 0.03\ M_\odot$. This implies that one needs to be cautious about interpreting the continuous mass ratio distribution (e.g., Jung et al. 2019a) as indicating a continuous planet mass distribution. That is, we need precise host masses for the many microlensing planets without $\pi_{\rm E}$ measurements in order to correctly understand the planet distribution beyond the snow line. Such host-mass measurements will be possible for the majority of microlensing planets detected to date at first AO light on next-generation (30 m) telescopes.

This research has made use of the KMTNet system operated by the Korea Astronomy and Space Science Institute (KASI) and the data were obtained at three host sites of CTIO in Chile, SAAO in South Africa, and SSO in Australia. Work by A.G. was supported by AST-1516842 from the US NSF. A.G. was supported by JPL grant 1500811. A.G. received support from the European Research Council under the European Unions

Seventh Framework Programme (FP 7) ERC grant Agreement No. [321035]. Work by C.H. was supported by grant 2017R1A4A1015178 of the National Research Foundation of Korea. Work by M.T.P. was partially supported by NASA grants NNX16AC62G and NNG16PJ32C. The OGLE has received funding from the National Science Centre, Poland, grant MAESTRO 2014/14/A/ST9/00121 to A.U. The MOA project is supported by JSPS KAKENHI grants No. JSPS24253004, JSPS26247023, JSPS23340064, JSPS15H00781, JP16H06287, and JP17H02871. UKIRT is currently owned by the University of Hawaii (UH) and operated by the UH Institute for Astronomy; operations are enabled through the cooperation of the East Asian Observatory. The collection of the 2018 data reported here was supported by NASA grant NNG16PJ32C and JPL proposal #18-NUP2018-0016. This research uses data obtained through the Telescope Access Program (TAP), which has been funded by the National Astronomical Observatories, Chinese Academy of Sciences, and the Special Fund for Astronomy from the Ministry of Finance. The work by W.Z., T.W., and S.M. is partly supported by the National Science Foundation of China (grant No. 11821303 and 11761131004 to SM).

ORCID iDs

Youn Kil Jung https://orcid.org/0000-0002-0314-6000
Jennifer C. Yee https://orcid.org/0000-0001-9481-7123
Yossi Shvartzvald https://orcid.org/0000-0003-1525-5041
Weicheng Zang https://orcid.org/0000-0001-6000-3463
Cheongho Han https://orcid.org/0000-0002-2641-9964
Sun-Ju Chung https://orcid.org/0000-0001-6285-4528
Kyu-Ha Hwang https://orcid.org/0000-0002-9241-4117
Yoon-Hyun Ryu https://orcid.org/0000-0001-9823-2907
In-Gu Shin https://orcid.org/0000-0002-4355-9838
Richard W. Pogge https://orcid.org/0000-0003-1435-3053
Jan Skowron https://orcid.org/0000-0002-2335-1730
Paweł Pietrukowicz https://orcid.org/0000-0002-2339-5899
Krzystof Ulaczyk https://orcid.org/0000-0001-6364-408X
Patryk Iwanek https://orcid.org/0000-0002-6212-7221
Sean Carey https://orcid.org/0000-0002-0221-6871
B. Scott Gaudi https://orcid.org/0000-0003-0395-9869
Calen B. Henderson https://orcid.org/0000-0001-8877-9060
David P. Bennett https://orcid.org/0000-0001-8043-8413
Akihiko Fukui https://orcid.org/0000-0002-4909-5763
Yoshitaka Itow https://orcid.org/0000-0002-8198-1968
Naoki Koshimoto https://orcid.org/0000-0003-2302-9562
Shota Miyazaki https://orcid.org/0000-0001-9818-1513
Nicholas J. Rattenbury https://orcid.org/0000-0001-5069-319X
Daisuke Suzuki https://orcid.org/0000-0002-5843-9433
Savannah Jacklin https://orcid.org/0000-0001-9504-8258
Matthew T. Penny https://orcid.org/0000-0001-7506-5640
Keivan G. Stassun https://orcid.org/0000-0002-3481-9052
Shude Mao https://orcid.org/0000-0001-8317-2788

References

Alard, C., & Lupton, R. H. 1998, ApJ, 503, 325
Albrow, M. D., Horne, K., Bramich, D. M., et al. 2009, MNRAS, 397, 2099
Albrow, M. D., Yee, J. C., Udalski, A., et al. 2018, ApJ, 858, 107
Bachelet, E., Beaulieu, J.-P., Boisse, I., Santerne, A., & Street, R. A. 2018, ApJ, 865, 162
Batista, V., Gould, A., Dieters, S., et al. 2011, A&A, 529, 102
Beaulieu, J.-P., Bennett, D. P., Fouqué, P., et al. 2006, Natur, 439, 437
Bensby, T., Yee, J. C., Feltzing, S., et al. 2013, A&A, 549, 147
Bessell, M. S., & Brett, J. M. 1988, PASP, 100, 1134
Bond, I. A., Abe, F., Dodd, R. J., et al. 2001, MNRAS, 327, 868
Calchi Novati, S., Gould, A., Udalski, A., et al. 2015a, ApJ, 804, 20
Calchi Novati, S., Gould, A., Yee, J. C., et al. 2015b, ApJ, 814, 92
Calchi Novati, S., Skowron, J., Jung, Y. K., et al. 2018, AJ, 155, 261
Calchi Novati, S., Suzuki, D., Udalski, A., et al. 2019, AJ, 157, 121
Chung, S.-J., Zhu, W., Udalski, A., et al. 2017, ApJ, 838, 154
Dominik, M. 1998, A&A, 329, 361
Dong, S., Gould, A., Udalski, A., et al. 2009, ApJ, 695, 970
Dong, S., Udalski, A., Gould, A., et al. 2007, ApJ, 664, 862
Gaudi, B. S. 1998, ApJ, 506, 533
Gaudi, B. S. 2012, ARA&A, 50, 411
Gould, A. 1992, ApJ, 392, 442
Gould, A. 1994, ApJL, 421, L75
Gould, A. 1997, in The Hollywood Strategy for Microlensing Detection of Planets, in Variables Stars and the Astrophysical Returns of the Microlensing Surveys, ed. R. Ferlet, J.-P. Maillard, & B. Raban (Gif-sur-Yvette: Editions Frontieres), 125
Gould, A. 2000, ApJ, 542, 785
Gould, A. 2004, ApJ, 606, 319
Gould, A. 2008, ApJ, 681, 1593
Gould, A., Carey, S., & Yee, J. 2013, Spitzer Proposal ID 10036, 10036
Gould, A., Carey, S., & Yee, J. 2014, Spitzer Proposal ID 11006, 11006
Gould, A., Carey, S., & Yee, J. 2016, Spitzer Proposal ID 13005, 13005
Gould, A., Dong, S., Bennett, D. P., et al. 2010, ApJ, 710, 1800
Gould, A., Yee, J., & Carey, S. 2015a, Spitzer Proposal ID 12013, 12013
Gould, A., Yee, J., & Carey, S. 2015b, Spitzer Proposal ID 12015, 12015
Gould, A., Yee, J., Carey, S., & Shvartzvald, Y. 2018, Spitzer Proposal ID 14012, 14012
Han, C., Hirao, Y., Udalski, A., et al. 2018, AJ, 155, 211
Han, C., Udalski, A., Lee, C.-U., et al. 2016, ApJ, 827, 11
Hwang, K.-H., Ryu, Y.-H., Kim, H.-W., et al. 2019, AJ, 157, 23
Hwang, K.-H., Udalski, A., Shvartzvald, Y., et al. 2018, AJ, 155, 20
Jiang, G., DePoy, D. L., Gal-Yam, A., et al. 2004, ApJ, 617, 1307
Jung, Y. K., Gould, A., Zang, W., et al. 2019a, AJ, 157, 72
Jung, Y. K., Han, C., Bond, I. A., et al. 2019b, ApJ, 872, 175
Jung, Y. K., Han, C., Gould, A., & Maoz, D. 2013, ApJL, 768, L7
Jung, Y. K., Han, C., Udalski, A., et al. 2018a, ApJ, 863, 22
Jung, Y. K., Udalski, A., Gould, A., et al. 2018b, AJ, 155, 219
Jung, Y. K., Udalski, A., Sumi, T., et al. 2015, ApJ, 798, 123
Jung, Y. K., Udalski, A., Yee, J. C., et al. 2017, AJ, 153, 129
Kayser, R., Refsdal, S., & Stabell, R. 1986, A&A, 166, 36
Kervella, P., Bersier, D., Mourard, D., et al. 2004, A&A, 428, 587
Kim, D.-J., Kim, H.-W., Hwang, K.-H., et al. 2018, AJ, 155, 76
Kim, S.-L., Lee, C.-U., Park, B.-G., et al. 2016, JKAS, 49, 37
Luri, X., Brown, A. G. A., Sarro, L. M., et al. 2018, A&A, 616, A9
Nataf, D. M., Gould, A., Fouqué, P., et al. 2013, ApJ, 769, 88
Paczyński, B. 1986, ApJ, 304, 1
Pejcha, O., & Heyrovský, D. 2009, ApJ, 690, 1772
Refsdal, S. 1966, MNRAS, 134, 315
Robin, A. C., Reylé, C., Derriére, S., & Picaud, S. 2003, A&A, 409, 523
Ryu, Y.-H., Yee, J. C., Udalski, A., et al. 2018, AJ, 155, 40
Schneider, P., & Weiss, A. 1987, A&A, 171, 49
Schönrich, R., Binney, J., & Dehnen, W. 2010, MNRAS, 403, 1829
Shin, I.-G., Udalski, A., Yee, J. C., et al. 2018, ApJ, 863, 23
Shvartzvald, Y., Bryden, G., Gould, A., et al. 2017a, AJ, 153, 61
Shvartzvald, Y., Yee, J. C., Calchi Novati, S., et al. 2017b, ApJL, 840, L3
Shvartzvald, Y., Yee, J. C., Skowron, J., et al. 2019, AJ, 157, 106
Skowron, J., Udalski, A., Gould, A., et al. 2011, ApJ, 738, 87
Street, R. A., Udalski, A., Calchi Novati, S., et al. 2016, ApJ, 819, 93
Sumi, T., Abe, F., Bond, I. A., et al. 2003, ApJ, 591, 20
Udalski, A. 2003, AcA, 53, 291
Udalski, A., Szymański, M. K., & Szymański, G. 2015a, AcA, 65, 1
Udalski, A., Yee, J. C., Gould, A., et al. 2015b, ApJ, 799, 237
Woźniak, P. R. 2000, AcA, 50, 421
Yee, J. C., Gould, A., Beichman, C., et al. 2015a, ApJ, 810, 155
Yee, J. C., Udalski, A., Calchi Novati, S., et al. 2015b, ApJ, 802, 76
Yoo, J., DePoy, D. L., Gal-Yam, A., et al. 2004, ApJ, 603, 139
Zang, W., Penny, M. T., Zhu, W., et al. 2018, PASP, 130, 104401
Zhu, W., Calchi Novati, S., Gould, A., et al. 2016, ApJ, 825, 60
Zhu, W., Udalski, A., Calchi Novati, S., et al. 2017, AJ, 154, 210
Zhu, W., Udalski, A., Gould, A., et al. 2015, ApJ, 805, 8